Radially polarized light in single particle optical extinction microscopy identifies silver nanoplates

Furqan Alabdullah ⓘ ; Vikramdeep Singh ⓘ ; Lukas Payne ⓘ ; David Regan ⓘ ; Francesco Masia ⓘ ; Victoria G. Rocha ⓘ ; Wolfgang Langbein ✉ ⓘ ; Paola Borri ⓘ

Check for updates

View Online   Export Citation

Radially polarized light in single particle optical extinction microscopy identifies silver nanoplates

View Online Export Citation CrossMark

Furqan Alabdullah,[1,2,3] (iD) Vikramdeep Singh,[4] (iD) Lukas Payne,[4] (iD) David Regan,[2] (iD) Francesco Masia,[2] (iD)
Victoria G. Rocha,[1,a)] (iD) Wolfgang Langbein,[4,b)] (iD) and Paola Borri[2] (iD)

AFFILIATIONS

[1]School of Engineering, Cardiff University, The Parade, Cardiff CF24 3AA, United Kingdom
[2]School of Biosciences, Cardiff University, Museum Avenue, Cardiff CF10 3AX, United Kingdom
[3]Engineering Technical College of Al-Najaf, Al-Furat Al-Awsat Technical University, Najaf 31001, Iraq
[4]School of Physics and Astronomy, Cardiff University, The Parade, Cardiff CF24 3AA, United Kingdom

[a)]Present address: Instituto de Ciencia y Tecnología Del Carbono (INCAR), CSIC, Francisco Pintado Fe 26, 33011 Oviedo, Spain.
[b)]Author to whom correspondence should be addressed: langbeinww@cardiff.ac.uk

ABSTRACT

Quantifying the optical extinction cross section of a single plasmonic nanoparticle (NP) has recently emerged as a powerful method to characterize the NP morphometry, i.e., size and shape, with a precision comparable to electron microscopy while using a simple optical microscope. Here, we enhance the capabilities of extinction microscopy by introducing a high numerical aperture annular illumination coupled with a radial polarizer to generate a strong axial polarization component. This enables us to probe the NP response to axial polarized light, and, in turn, to distinguish flat-lying nanoplates from other geometries. Polarization-resolved optical extinction cross sections were acquired on 219 individual colloidal silver NPs of a nominally triangular nanoplate shape but, in practice, exhibiting heterogeneous morphometries, including decahedrons and non-plate spheroids. An unsupervised machine learning cluster analysis algorithm was developed, which allowed us to separate NPs into different groups, owing to the measured differences in cross sections. Comparison of the measurements with a computational model of the absorption and scattering cross section accounting for nanoplates of varying geometries beyond simple triangles provided insight into the NP shape of each group. The results provide a significant improvement of polarization-resolved optical extinction microscopy to reconstruct NP shapes, further boosting the utility of the method as an alternative to electron microscopy analysis.

Metallic nanoparticles (NPs) are attracting increasing attention owing to their strong light absorption and scattering at localized surface plasmon resonances (LSPRs), with applications ranging from chemical sensing, via, e.g., surface-enhanced Raman (SERS) scattering,[1] to photovoltaics,[2] and photothermal biomedical therapies.[3] Both gold and silver have been widely investigated since they have a material permittivity allowing to realize NPs with LSPRs in the visible and near infrared wavelength range. While gold NPs are more biocompatible and chemically stable, silver NPs exhibit superior optical properties. This is a result of lower non-radiative damping owing to a smaller imaginary part of the permittivity for silver compared to gold, as a result of lower Drude damping and the absence of interband transitions in the visible range.[4] In turn, silver NPs show stronger and spectrally sharper LSPR optical extinction cross sections and higher local field enhancement effects for sensing applications.

Using colloidal synthesis, metallic NPs can be fabricated with a large variety of shapes and sizes. Particularly in the context of SERS applications, much attention is given to the production of tip-shaped NPs, owing to the formation of high local fields near sharp tips. To that end, silver triangular nanoplates have been extensively investigated.[5–7] One of the challenges in the fabrication of these nanotriangles is the control of their size and shape distribution,[7] which, in turn, requires reliable morphometric analysis techniques.

Complementing electron microscopy, which is costly and time-consuming, significant effort has been devoted to developing NP analysis techniques using optical microscopy methods.[8–10] For example, polarization and spectrally resolved dark-field microscopy has been used to analyze the in-plane anisotropy of various plasmonic NPs.[8] The length and diameter of gold nanorods have been determined from the LSPR position and width in scattering spectra.[11,12] Quantitative

techniques able to provide optical cross sections[13,14] or the complex polarizability[15] of a NP are particularly attractive, as these physical quantities can be linked to the NP size and shape. In that context, we have recently demonstrated a rapid and quantitative method for NP morphometric analysis based on measuring the polarization-resolved wavelength-dependent optical extinction cross section of single NPs.[16] Notably, while single particle analysis methods overcome the limitations of ensemble averaged approaches, they need to be implemented in a high throughput fashion to provide statistically relevant information on size and shape distributions, especially for heterogeneous populations of NPs. Our method offers this key capability, as it is based on wide-field transmission microscopy with hundreds of individual NPs simultaneously imaged in the field of view. To date, we have applied this polarization-resolved optical extinction micro-spectroscopy analysis to gold NPs having quasi-spherical or rod-like shapes in 3D and relatively narrow size and shape distributions.[16,17]

In the present work, we enhance the capabilities of the extinction microscopy method to investigate a heterogeneous population of silver triangular nanoplates. Nominally, these NPs have 40 nm diameter and 10 nm thickness, but, in practice, exhibit a variety of shapes and sizes as observed in transmission electron microscopy (TEM). Notably, in our published method,[16] a set of linear excitation polarizations was used to provide information on the in-plane polarization dependence of the NP extinction. However, the axial polarization component, which facilitates examination of the NP polarizability in the axial direction, was small and not changing within the set. This shortcoming was recognized in the analysis of the three-dimensional orientation and shape of quasi-spherical gold NPs[16] but is even more relevant for nanoplates, which present a strongly different response for light polarization normal to the plate. Considering that plates are preferentially lying flat on a planar substrate, the axial polarization direction is important to identify the plate morphology. Therefore, in addition to the linear excitation polarizations, we introduce here a configuration consisting of a high numerical aperture (NA) annular ring illumination coupled with a radial polarizer to generate a strong axial polarization component.

Polarization-resolved optical extinction cross sections were acquired on 219 individual NPs, and an unsupervised machine learning cluster analysis algorithm was developed and applied to the data, which allowed us to separate NPs into different groups, owing to the measured differences in wavelength and polarization dependent cross sections. Notably, while unsupervised cluster analysis approaches have been reported in the literature for TEM data,[18,19] their application to optical extinction microscopy has not been shown to date. A comprehensive framework of numerical simulations was then developed for the cross-section spectra of nanoplates with varying geometries, going beyond previous models,[6,20] and providing the characteristic sizes and shapes within the nanoplate groups.

A sketch of the microscope setup and sample geometry is shown in Fig. 1, and more details are given in the supplementary material, Sec. S3. Measurements were performed on a Nikon Ti-U inverted microscope using illumination wavelengths λ covering the range from 500 to 750 nm in 50 nm steps. The light polarization was controlled, either by a rotatable linear polarizer at an angle γ_P using an illumination numerical aperture NA of 1.34, or by a radial polarizer (see Sec. S3 ii) using an annular NA of 1.00–1.34 (see Sec. S3 iii) to increase the axial polarization component of the illumination. The sample position was controlled by a piezoelectric stage, and the transmitted light was imaged onto a camera.
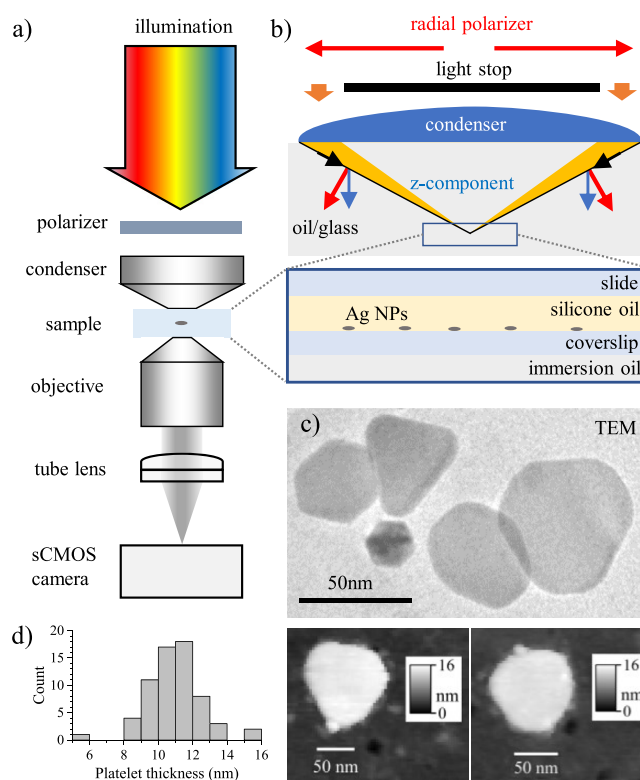

FIG. 1. Sketch of the microscope setup and investigated sample. (a) Under Köhler illumination of a selectable wavelength range, the sample is imaged onto a camera, using a 1.34 NA condenser and a 1.45 NA objective. (b) In the illumination, a rotatable linear polarizer or a radial polarizer with a light stop in the back focal plane of the condenser is used; the latter generating a significant axially polarized illumination component in the focal plane. The sample consists of individual silver nanoplates deposited onto a glass coverslip, surrounded by silicone oil index matched to glass. (c) Example transmission electron microscopy (TEM) image illustrating the variety of nanoplate sizes and shapes in the sample. (d) Nanoplates deposited on the glass coverslip measured with AFM, showing statistics of measured heights and two examples of AFM topographies.

We investigated nominally triangular silver nanoplates (nanoComposix) protected by a polyvinylpyrrolidone (PVP) capping polymer to increase steric stability in 5 mM sodium borate buffer. Choosing an appropriate dilution from the stock, NPs were deposited onto a cleaned glass coverslip by a wet casting method (see Sec. S1). The deposition resulted in an average particle distance of a few micrometers on the surface, well above the diffraction limited spatial resolution in the microscope, such that individual NPs were separated in the field of view (see Fig. S8). NPs were surrounded by silicone oil matching the refractive index of glass ($n = 1.52$), covered with a glass slide and sealed by nail varnish (see Fig. S1).

An example of the size and shape of the investigated NP type is shown in the TEM image in Fig. 1(c) (additional TEM images are shown in Fig. S2). While specified as triangular plates of 40 nm diameter and 10 nm thickness, a variety of sizes and shapes are observed, including hexagonal and tip-truncated triangular plates, decahedra, and spheroids. Atomic force microscopy images of nanoplates deposited on the coverslip are given in Fig. 1(d). They show a height

distribution centered around 11 nm and hence an average silver thickness of 5–9 nm taking into account a 1–3 nm thick PVP surfactant layer[21] on both sides. The ensemble average optical absorbance spectrum of the stock (see Fig. S4) has a main LSPR centered at 660 nm of 175 nm full-width at half maximum (FWHM), a weaker band around 400–450 nm, and an even weaker peak at 340 nm. By comparison with literature,[22,23] the main LSPR peak can be attributed to the in-plane dipole mode, the 400–450 nm band to the in-plane quadrupole mode, and the 340 nm peak to the out-of-plane dipole mode. The large FWHM of the main LSPR is consistent with the NP size and shape distribution, as the in-plane dipole resonance wavelength redshifts with increasing triangle edge length and decreasing plate thickness.[6] Small quasi-spherical silver NPs exhibit an LSPR around 410 nm in water,[24] contributing to the 400–450 nm band.

Exemplar optical extinction cross-section spectra of single NPs are shown in Fig. 2. The method to quantitatively extract an extinction cross section σ from the measured wide-field transmission image was described in our previous works[16,25] and is detailed in Sec. S3 iv. We use a shifted reference technique, whereby two transmission images are taken with the sample laterally moved by a small distance and one is referenced to the other. Resulting extinction contrast images Δ_1 for a selected NP are shown in Fig. 2(a) for linear and radial polarizations (see Fig. S8 for a full field of view), showing a bright spot at one NP position and a dark spot at the other. A marked reduction of contrast from linear to radial polarization is observed. The spectra of σ of the NPs were measured for linear polarization at $\gamma_P = 0°, 45°, 90°, 135°$ and for radial polarization. Figure 2(b) shows the results for the selected NP, indicating a negligible dipolar in-plane asymmetry (no significant differences are observed vs γ_P), a main LSPR at 650 nm, and a reduction of σ by about a factor of 2 from linear to radial polarizer. The spectra of another NP with a markedly different behavior are

FIG. 2. (a) Optical extinction contrast image Δ_1 of a selected individual NP, acquired at $\lambda = 650$ nm using the linear polarizer at $\gamma_P = 0°$ or the radial polarizer, as indicated. (b) Extinction cross-section spectra for the NP in (a), at different linear polarizer angles and with the radial polarizer, as indicated. (c) Extinction cross-section spectra as in (b) but for a different NP. The inset shows the cross section at $\lambda = 500$ nm vs γ_P, with a sinusoidal fit providing parameters as indicated.

shown in Fig. 2(c), having an LSPR below 500 nm, a clear dependence on γ_P and comparable values for linear and radial polarizers. In the inset of Fig. 2(c), the dependence on γ_P at $\lambda = 500$ nm is shown and fitted using the function $\sigma_L(1 + \alpha \cos(2(\gamma_P - \gamma)))$. The corresponding fit parameters are indicated, with errors taking into account the measurement noise, as discussed in Ref. 16.

The observed differences are due to the different morphometry of the two NPs. The spectra in Fig. 2(b) are consistent with a small thin triangular nanoplate, while the spectra in Fig. 2(c) suggest a spheroidal NP which has in-plane dipolar asymmetry. Regarding the measured changes from linear to radial polarization in Fig. 2(b), calculations[23] show that the absorption cross-section spectrum of a thin nanoplate in the wavelength range of the main dipole LSPR mode is negligible for axially polarized light. Under the excitation conditions used, we have determined the relative intensity of the illumination components on the sample which are in-plane ($I_\parallel, I_\perp$) and axially (I_z) polarized, as discussed in Ref. 16. Using the linear polarizer and 0 to 1.34 NA, we find $I_{\parallel,L} = 0.825$, $I_{\perp,L} = 0.007$, $I_{z,L} = 0.168$, where $\parallel$ indicates the direction along the polarizer axis and $\perp$ orthogonal to it. Conversely, with the radial polarizer and annular illumination from 1.00 to 1.34 NA, we obtain $I_{\parallel,R} = I_{\perp,R} = 0.209$ and $I_{z,R} = 0.582$. We also note that the data are affected by the long shadow effect,[26] providing a correction factor for the measured optical cross sections of about 1.25 for 0–1.34 NA and about 1.6 for 1.00–1.34 NA. This implies that the measured σ_R to σ_L ratio carries a factor of 1.28.

The spectra in Fig. 2(b) show that σ at the LSPR peak at $\lambda = 650$ nm is decreased using the radial polarizer to about 44% of the value for the linear polarizer. This is consistent with having a nanoplate lying flat on the substrate and, therefore, exhibiting a negligible extinction at the LSPR for axial polarization. For the NP in Fig. 2(c) instead, the cross section using radial and linear polarizations are similar, indicating a spheroidal NP of similar size in axial and in-plane directions.

Measurements of σ vs λ, both with linear polarization at four γ_P and with the radial polarization as in Fig. 2 were carried out in multiple sample regions providing a total of 219 analyzed individual NPs, and an overview of the results is shown in Fig. S9. We observe a widely distributed behavior, reflecting the variety of shapes and sizes in the sample seen in TEM. Owing to the rich information available from the measurements, we applied an unsupervised cluster analysis to separate NPs into groups representing distinct particle morphometries. For the analysis, each NP is described by a 18-dimensional predictor given by the wavelength-resolved values of $\tilde{\sigma}_L$, $2\alpha\tilde{\sigma}_L$ and $\tilde{\sigma}_R$, where $\tilde{\sigma}_L$ and $\tilde{\sigma}_R$ are the cross sections for linear and radial polarization normalized to the mean $\bar{\sigma}$ of all cross sections measured for the NP across wavelengths and polarizations. This normalization removes the absolute cross-sectional information which mainly encodes for particle size rather than shape. A hierarchical cluster analysis (HCA) using a cosine metric and average linkage was used. We show here the results for nine groups as they provide a separation of nanoplates of different LSPR wavelength ranges. In Fig. 3(a), the values of the first two components of a principal component analysis (PCA) of the predictors over the NP ensemble are shown, with the groups identified by colors. The corresponding dendrogram is shown in Fig. S12 and a histogram of $\bar{\sigma}$ in each group is shown in Fig. S10. The groups sort the NPs into adjacent regions, indicating a rather continuous distribution of shapes. Clustering results using different number of groups, metrics, and
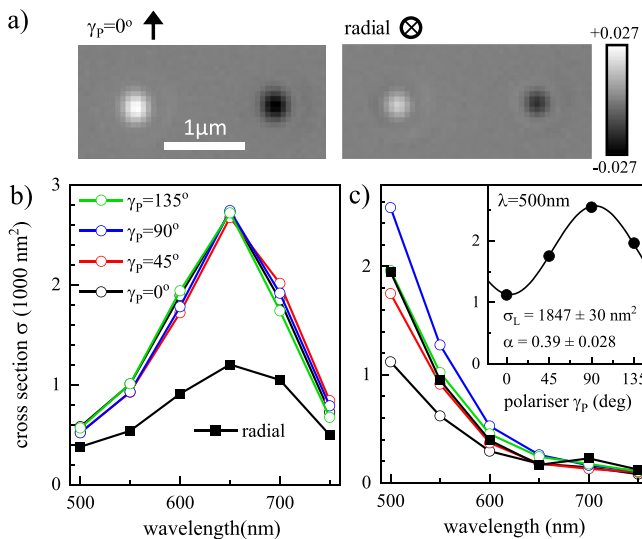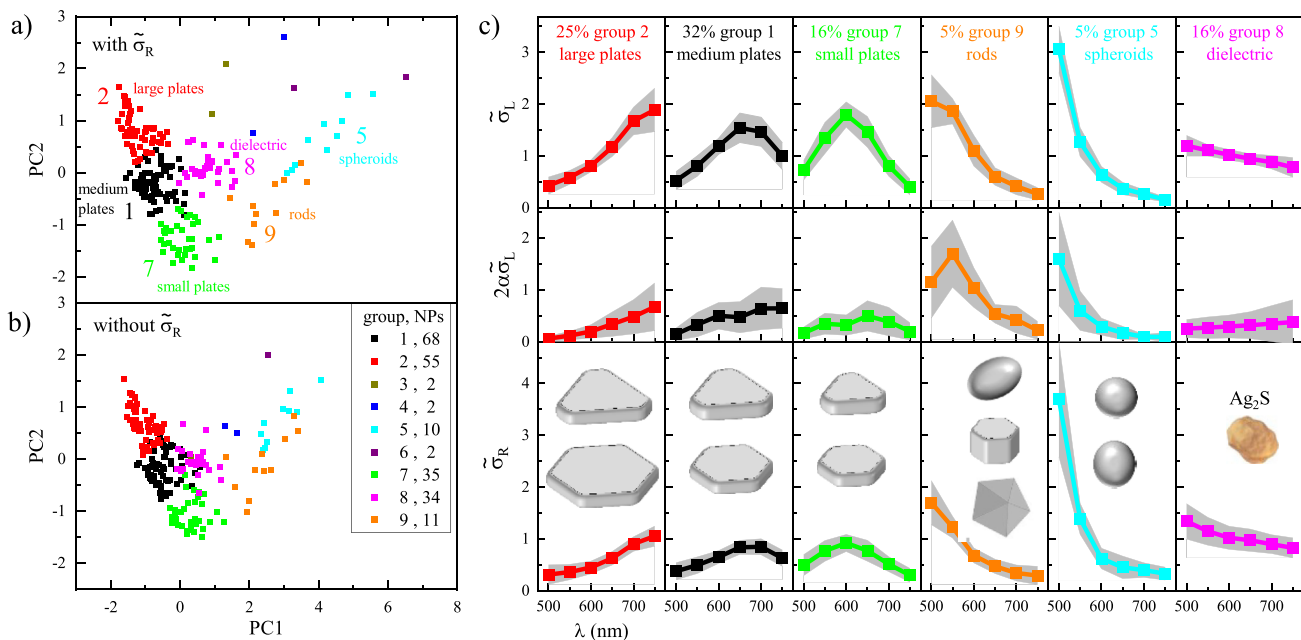
FIG. 3. Results of cluster analysis. (a) NP predictor first and second principal component values. The symbol color indicates the group, with group number and naming indicated. (b) as (a), but excluding $\tilde{\sigma}_R$ from the PCA. The number of NPs in each group is given. (c) Spectra of the predictors for groups containing more than two NPs. Symbols show the average and the shaded area shows the standard deviation over the NPs in the group. The percentage of NPs in each group is given. Sketches of possible shapes are provided for illustration.

linkages are provided in Sec. S4. Notably, in the principal components excluding the radial polarizer data [Fig. 3(b)], the groups partially overlap, and also repeating the HCA excluding the radial polarizer data results in a poorer separation of the plate-like NPs (see Fig. S15). Introducing the magnitude of the measured cross section as a predictor does not improve the separation of the groups as shown in Fig. S16.

The average spectra of the predictors for each group given in Fig. 3(c) show distinctive features reporting the corresponding NP properties. Clusters 2, 1, and 7 have a dominant $\tilde{\sigma}_L$, with a small α_L around 0.2, and $\tilde{\sigma}_R$ about half of $\tilde{\sigma}_L$, indicating flat lying nanoplates. The difference between these groups is the LSPR wavelength, moving from a center of 750 nm in group 2 to 670 nm in group 1, and to 600 nm in group 7. These three nanoplate groups represent the majority of NPs, 72% of the ensemble, and are called large, medium, and small plates in the following. This is consistent with about 70% of NPs found to be plates in TEM (see Sec. S2 i).

Group 9 has LSPRs around 500 nm and shows a large α_L around one, while $\tilde{\sigma}_R$ is only slightly lower than $\tilde{\sigma}_L$. This group, thus, contains particles elongated in-plane, e.g., bipyramids or decahedra lying tilted on the surface,[27] and it is called rods in the following. Cluster 5 is similar to group 9, but with LSPRs further shifted to the blue, below 500 nm, outside of the measured range, indicating a quasi-spherical shape, and is called spheroids in the following. Notably, $\tilde{\sigma}_R$ is somewhat larger than $\tilde{\sigma}_L$, and α_L is reduced to around 0.5, which could indicate close to hexagonal pillars, i.e., plates thicker than wide, standing upright, similar to the about 25 nm diameter one seen in the TEM in Fig. 1, or spheroids with a longer axis out-of-plane. The long shadow effect mentioned before allows for $\tilde{\sigma}_R$ being 28% larger than $\tilde{\sigma}_L$ for a spherical NP.

Cluster 8 instead shows a different behavior—a nearly isotropic cross section (small α_L, and $\tilde{\sigma}_R$ similar to $\tilde{\sigma}_L$), and no LSPR but a slowly increasing cross section with decreasing wavelength. This points toward absorbing dielectric particles, possibly Ag_2S, which is the predominant product of silver decomposition (also known as tarnish), or air bubbles in the oil medium. The group is called dielectric in the following. More discussion is given in Sec. S5.

Spectra of selected NPs from the nanoplate groups are shown in Fig. 4. To provide a quantitative comparison of the measured cross-sectional spectra with theoretical expectations, we have simulated the scattering and absorption spectra of silver nanoplates using the finite element solver COMSOL. A flexible geometrical model was developed including edge and corner radii, thickness, and separate distances of all six edges from the center of the plate, allowing us to describe general asymmetric hexagons, as detailed in Sec. S6. Here, we compare the calculated cross sections of nanoplates of a given geometry with selected NPs. An edge rounding of 2 nm and a corner rounding of 5 nm was used throughout. For group 2, the selected NP has an LSPR around 710 nm with a small polarization splitting and a rather large peak cross section around 6000 nm^2. The simulated spectra show good agreement with the measurements for both linear and radial polarizers, assuming a nearly hexagonal nanoplate of 6.3 nm height and center-to-edge distances of 24 nm along x and 23 nm for the other distances. For group 1, two NPs were selected. NP #1 shows no polarization splitting of the LSPR at 650 nm, agreeing with simulated spectra of a hexagonal nanoplate of 5.4 nm height and 16.5 nm center to edge distance. A triangular geometry can also model the spectra (see Fig. S22), albeit with somewhat worse agreement at 500 nm. NP #2 instead shows a strong polarization splitting of the LSPR with peaks at 710 and 610 nm,
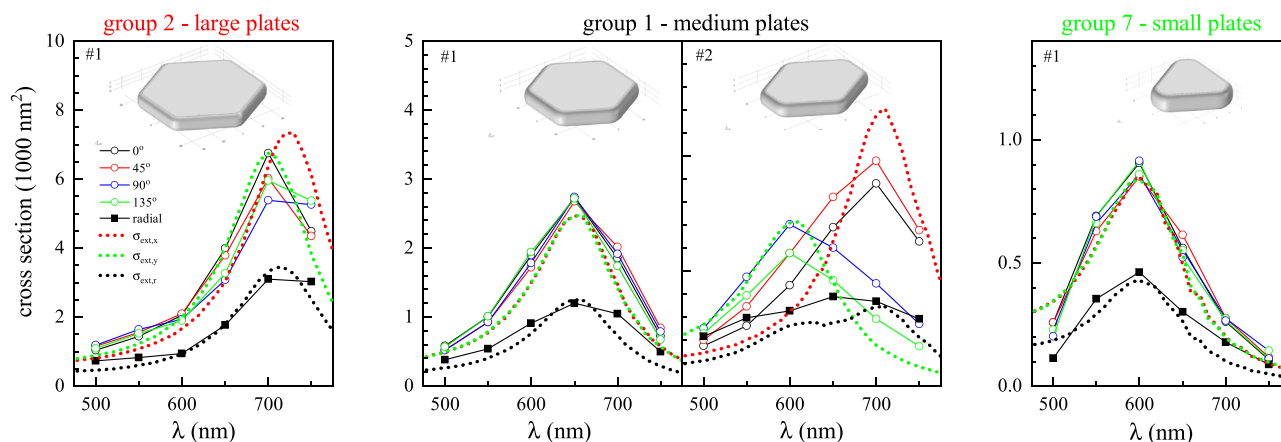
FIG. 4. Cross-section spectra of selected NPs from groups attributed to large, medium, and small plates, as labeled. Measured spectra for linear polarization at four angles γ_P (circles) and for the radial polarizer (squares). Simulated spectra (dotted lines) for geometries chosen to approximate the measured spectra are shown, together with their geometries (for details and NP parameters, see text and Sec. S6). Spectra are shown for the linear polarizer along the longer wavelength LSPR axis x (red), the shorter wavelength LSPR axis y (green), and for the radial polarizer (black).

indicating an elongated plate. The simulated spectra of a nanoplate of 5 nm height, 18 nm center-to-edge distance along x and 14 nm for the other distances show good agreement with the measurements. For group 7, the selected NP exhibits no polarization splitting of the LSPR at 650 nm and agrees with simulated spectra of a triangular nanoplate of 6.1 nm height and alternating 10 and 14 nm center to edge distances. An hexagonal geometry can also model the spectra, but with a thickness below 5 nm. More information, including scattering and absorption spectra and local field distributions, are given in Sec. S6. Notably, the sizes of the simulated plates between 24 and 47 nm are consistent with the size distribution of plates found by TEM shown in Fig. S3.

In conclusion, we have demonstrated a quantitative extinction micro-spectroscopy analysis, which combines wavelength-resolved radially and linearly polarized illumination as a powerful tool to distinguish silver nanoplates from other shapes. We examined a heterogeneous population of individual silver NPs and showed that the measured 18 dimensional cross-sectional data enabled the application of an unsupervised cluster analysis to separate NPs into morphometrically distinct groups. A computational model of the absorption and scattering cross section of nanoplates was developed, covering a wide range of possible shapes. The quantitative comparison between calculated and measured cross sections then provided useful insight into consistent nanoplate shapes. Owing to the simplicity of optical extinction micro-spectroscopy, the method provides an interesting alternative to taxing electron microscopy for single particle morphometric analysis.

See the supplementary material for details regarding the sample preparation (Sec. S1) and additional sample characterization (Sec. S2); details on the extinction microscopy, including the optical setup, the linear and radial polarizer, the dark-field disk, and the data acquisition and analysis (Sec. S3); details and further results concerning the cluster analysis, including group separation, dendrograms, different number of groups, linkages, metrics, removing radial polarizer descriptors and including a magnitude term (Sec. S4); modeling of dielectric NPs (Sec. S5); and details of the modeling of the

nanoplate extinction, covering the geometry, the electromagnetic model, and showing additional results including spectra along the transition from hexagonal to triangular shape, and polarization resolved spectra for selected geometries with corresponding spatial field distributions (Sec. S6).

AUTHOR DECLARATIONS
Conflict of Interest

The authors have no conflicts to disclose.

Author Contributions

Furqan Alabdullah: Data curation (lead); Formal analysis (lead); Funding acquisition (equal); Investigation (lead); Methodology (supporting); Validation (lead); Visualization (equal); Writing – original draft (supporting); Writing – review & editing (supporting). **Vikramdeep Singh:** Data curation (supporting); Formal analysis

DATA AVAILABILITY

Information on the data underpinning the results presented here, including how to access them, can be found in the Cardiff University data catalogue at https://doi.org/10.17035/d.2023.0295639845.

REFERENCES

[1] Q. Li, H. Huo, Y. Wu, L. Chen, L. Su, X. Zhang, J. Song, and H. Yang, "Design and synthesis of SERS materials for in vivo molecular imaging and biosensing," Adv. Sci. **10**, 2202051 (2023).

[2] H. A. Atwater and A. Polman, "Plasmonics for improved photovoltaic devices," Nat. Mater. **9**, 205–213 (2010).

[3] N. S. Abadeer and C. J. Murphy, "Recent progress in cancer thermal therapy using gold nanoparticles," J. Phys. Chem. C **120**, 4691–4716 (2016).

[4] S. Babar and J. H. Weaver, "Optical constants of Cu, Ag, and Au revisited," Appl. Opt. **54**, 477–481 (2015).

[5] L. J. Sherry, R. Jin, C. A. Mirkin, G. C. Schatz, and R. P. V. Duyne, "Localized surface plasmon resonance spectroscopy of single silver triangular nanoprisms," Nano Lett. **6**, 2060–2065 (2006).

[6] M. G. Blaber, A.-I. Henry, J. M. Bingham, G. C. Schatz, and R. P. V. Duyne, "LSPR imaging of silver triangular nanoprisms: Correlating scattering with structure using electrodynamics for plasmon lifetime analysis," J. Phys. Chem. C **116**, 393–403 (2012).

[7] A. L. Beulze, E. Duguet, S. Mornet, J. Majimel, M. Tréguer-Delapierre, S. Ravaine, I. Florea, and O. Ersen, "New insights into the side-face structure, growth aspects, and reactivity of Ag$_n$ nanoprisms," Langmuir **30**, 1424–1434 (2014).

[8] O. Schubert, J. Becker, L. Carbone, Y. Khalavka, T. Provalska, I. Zins, and C. Sönnichsen, "Mapping the polarization pattern of plasmon modes reveals nanoparticle symmetry," Nano Lett. **8**, 2345–2350 (2008).

[9] A. Crut, P. Maioli, N. D. Fatti, and F. Vallée, "Optical absorption and scattering spectroscopies of single nano-objects," Chem. Soc. Rev. **43**, 3921–3956 (2014).

[10] J. Olson, S. Dominguez-Medina, A. Hoggard, L.-Y. Wang, W.-S. Chang, and S. Link, "Optical characterization of single plasmonic nanoparticles," Chem. Soc. Rev. **44**, 40–57 (2015).

[11] A. Henkel, W. Ye, Y. Khalavka, A. Neiser, C. Lambertz, S. Schmachtel, R. Ahijado-Guzmán, and C. Sönnichsen, "Narrowing the plasmonic sensitivity distribution by considering the individual size of gold nanorods," J. Phys. Chem. C **122**, 10133–10137 (2018).

[12] K. Shiratori, L. D. C. Bishop, B. Ostovar, R. Baiyasi, Y.-Y. Cai, P. J. Rossky, C. F. Landes, and S. Link, "Machine-learned decision trees for predicting gold nanorod sizes from spectra," J. Phys. Chem. C **125**, 19353–19361 (2021).

[13] M. Husnik, S. Linden, R. Diehl, J. Niegemann, K. Busch, and M. Wegener, "Quantitative experimental determination of scattering and absorption cross-section spectra of individual optical metallic nanoantennas," Phys. Rev. Lett. **109**, 233902 (2012).

[14] S. Adhikari, P. Spaeth, A. Kar, M. D. Baaske, S. Khatua, and M. Orrit, "Photothermal microscopy: Imaging the optical absorption of single nanoparticles and single molecules," ACS Nano **14**, 16414–16445 (2020).

[15] S. Khadir, D. Andrén, P. C. Chaumet, S. Monneret, N. Bonod, M. Käll, A. Sentenac, and G. Baffou, "Full optical characterization of single nanoparticles using quantitative phase imaging," Optica **7**, 243–248 (2020).

[16] L. M. Payne, W. Albrecht, W. Langbein, and P. Borri, "The optical nanosizer—Quantitative size and shape analysis of individual nanoparticles by high-throughput widefield extinction microscopy," Nanoscale **12**, 16215–16228 (2020).

[17] L. M. Payne, F. Masia, A. Zilli, W. Albrecht, P. Borri, and W. Langbein, "Quantitative morphometric analysis of single gold nanoparticles by optical extinction microscopy: Material permittivity and surface damping effects," J. Chem. Phys. **154**, 044702 (2021).

[18] X. Wang, J. Li, H. D. Ha, J. C. Dahl, J. C. Ondry, I. Moreno-Hernandez, T. Head-Gordon, and A. P. Alivisatos, "AutoDetect-mNP: An unsupervised machine learning algorithm for automated analysis of transmission electron microscope images of metal nanoparticles," JACS Au **1**, 316–327 (2021).

[19] H. Wen, J. M. Luna-Romera, J. C. Riquelme, C. Dwyer, and S. L. Y. Chang, "Statistically representative metrology of nanoparticles via unsupervised machine learning of TEM images," Nanomaterials **11**, 2706 (2021).

[20] R. Jin, Y. Cao, C. A. Mirkin, K. L. Kelly, G. C. Schatz, and J. G. Zheng, "Photoinduced conversion of silver nanospheres to nanoprisms," Science **294**, 1901–1903 (2001).

[21] J. Hwang, Y. Shim, S.-M. Yoon, S. H. Lee, and S.-H. Park, "Influence of polyvinylpyrrolidone (PVP) capping layer on silver nanowire networks: Theoretical and experimental studies," RSC Adv. **6**, 30972–30977 (2016).

[22] K. L. Kelly, E. Coronado, L. L. Zhao, and G. C. Schatz, "The optical properties of metal nanoparticles: The influence of size, shape, and dielectric environment," J. Phys. Chem. B **107**, 668–677 (2003).

[23] F. K. Guedje, M. Giloan, M. Potara, M. N. Hounkonnou, and S. Astilean, "Optical properties of single silver triangular nanoprism," Phys. Scr. **86**, 055702 (2012).

[24] B. J. Wiley, S. H. Im, Z.-Y. Li, J. McLellan, A. Siekkinen, and Y. Xia, "Maneuvering the surface plasmon resonance of silver nanostructures through shape-controlled synthesis," J. Phys. Chem. B **110**, 15666–15675 (2006).

[25] L. M. Payne, W. Langbein, and P. Borri, "Wide-field imaging of single-nanoparticle extinction with sub-nm^2 sensitivity," Phys. Rev. Appl. **9**, 034006 (2018).

[26] L. Payne, A. Zilli, Y. Wang, W. Langbein, and P. Borri, "Quantitative high-throughput optical sizing of individual colloidal nanoparticles by wide-field imaging extinction microscopy," Proc. SPIE **10892**, 108920J (2019).

[27] Y. Wang, Z. Sztranyovszky, A. Zilli, W. Albrecht, S. Bals, P. Borri, and W. Langbein, "Quantitatively linking morphology and optical response of individual silver nanohedra," Nanoscale **14**, 11028–11037 (2022).

03 May 2024 15:12:33